

Sulfur solubility in a deep magma ocean and implications for the deep sulfur cycle

E.S. Steenstra, O. Lord, S. Vitale, E.S. Bullock, S. Klemme, M. Walter

Supplementary Information

The Supplementary Information includes:

- S.1 Experimental and Analytical Details
- S.2 Evidence for Sulfide-saturation of Experimental Silicate Melts
- S.3 Correcting SCSS values for Variable Silicate Melt FeO Contents
- S.4 Non FeO-compositional Effects on Derived SCSS values
- S.5 Dataset used for Parameterisations
- S.6 Modelling Approach
- Tables S-1 and S-2
- Figures S-1 to S-3
- Supplementary Information References

S.1 Experimental and Analytical Details

To study the solubility of S in a deep terrestrial magma ocean, sulfide liquids and silicate melts were equilibrated at pressures of 35–40 GPa and temperatures between 3925–4600 K in a laser-heated diamond anvil cell (DAC). The sulfide powder consisted of FeS and 3 wt. % of trace elements (ESS-DAC-4: FeS + 2 wt. % Cu and 1 wt. % Se; ESS-DAC-5: FeS + 2 wt. % Cu and 1 wt. % Te; ESS-DAC-7: FeS + 1.5 wt. % Cd and 1.5 wt. % Sn). The silicate powder consisted of a grounded (from glass), synthetic equivalent of a mean MORB basaltic composition (Table S-1, Gale *et al.*, 2013). The MORB silicate composition was used because it quenches to a glass and because its melting temperature is significantly lower than more magnesian compositions. In addition, it also allows for direct comparison with data that was obtained over



much larger P - T ranges due to its lower melting point and extensive use in past low-pressure studies. The glass was produced by mixing the appropriate amounts of high-purity carbonates and oxides under ethanol in an agate mortar for 30 minutes. The mixture was then decarbonated over 6-7 hours from 923 to 1273 K, taken from the furnace and subsequently melted at 1723 K for 15 minutes in a box furnace.

Experiments were performed in Princeton-type symmetric cells, equipped with anvils with culets of 250 μm diameter. Sample chambers of diameter 85 μm were laser drilled in 250 μm thick Re gaskets pre-indented to a thickness of 50 μm . Powdered starting materials were pressed between two opposing diamonds with culet diameters of 500 μm to produce thin foils \sim 10 to 15 μm thick. A piece of the sulfide wafer \sim 20 μm across was loaded into the sample chamber between pieces of the MORB wafer chosen to closely match the diameter of the sample chamber. In this geometry, the MORB acts as the pressure medium and thermal insulation.

The fluorescence signal from a ruby grain loaded into the sample chamber but away from the heated region was used to monitor the pressure during pressurisation and after heating. Pressures were calculated using two different approaches. In the first method the reported pressures are the average between pre-heating and post-heating measurements. In the second approach, we took into account the potentially important thermal pressure effects using the parameterisation of Siebert *et al.* (2012):

$$\Delta P_{\text{th}} \sim 2.7^{-3} \text{ GPa/K} \quad \text{Eq. (S-1)}$$

These calculations showed pressures were between 43 to 53 GPa during the experiment (Table 1 in the main text); these values were used throughout the study. The pressure uncertainty is estimated to be approximately 2 GPa at the conditions of the experiments (Walter *et al.*, 2015). Samples were heated at high pressure using the double-sided pulsed laser heating system at the School of Earth Sciences, University of Bristol and described in detail in Lord *et al.* (2014). Samples were heated with a pair of 100-W Yb-doped fibre lasers for approximately 60 to 180 seconds, by switching on the lasers at a high power during which a steady state must have been achieved, given previous results for LH-DAC partitioning experiments (*e.g.* Suer *et al.*, 2017; Mahan *et al.*, 2018). Samples were quenched by switching off the power to the lasers. During this period, multiple 1-D temperature transects were measured across both sides of the heated spot using the optical system also described in Lord *et al.* (2014) and standard spectroradiometric techniques (Walter and Koga, 2004). Reported temperatures are an average of the peak temperatures of each of these transects and the reported uncertainty is their standard deviation.

Recovered experimental run products were mounted on Si wafers. Cross-sections of experimental charges were made using a dual beam FEI Helios G4 Xe PFIB at the Earth and Planets Laboratory, Carnegie Institution for Science. A 5 μm protective layer of tungsten (W) was deposited on to the sample surface. Standard FIB cross sectioning techniques were used over a current range of 60 nA to 2.5 μA . Samples were finished with 30 kV Xe ions. Final sample thicknesses were approximately 20 μm . Run products were carbon-coated and analysed using an EPMA at the latter institution.

Major and trace element compositions of the silicate melts and/or sulfide liquids were obtained using a JEOL JXA 8530F field emission electron microprobe at the Earth and Planets Laboratory, Carnegie Institution for Science. Analyses were performed using a defocused beam of mostly 1 μm and occasionally 3 μm diameter. Measurement points were set in random lines and/or raster grids, depending on the available surface area of the analysed phases. Beam currents were 20 nA with an accelerating voltage of 15 kV. Dwell times were 10–40 s on peak and 5–20 s on each background. Standards used were anorthite for Ca, Fe metal or fayalite for Fe, San Carlos olivine for Si, orthoclase for K, albite or DJ35 for Na, PbS or pyrite for S, TiO₂ or pure metal for TiO₂, SnSe for Se, CdTe for Cd and pure metal standards for Cu, and Re. Calibrations were considered successful when the primary standard compositions were reproduced within 1% relative



deviation. Data reduction was performed using the ZAF correction, which corrects for the decrease in x-ray density due to the distance the x-rays travel through the specimen before they reach the detector. In runs ESS-4 and ESS-5 the sulfide liquid was either too small to measure or migrated too far from the hotspot due to its very low viscosity at such conditions.

Special care was taken to not measure too close to sulfide liquid ($>15\ \mu\text{m}$, and usually much further away), as this would potentially yield secondary fluorescence effects on measured S abundances, as observed for other elements such as Ni (Wade and Wood, 2012). Wafer (sample) thickness may also result in analytical uncertainties, as not all photons that are emitted would arrive at the detector, due to deeper penetration of electrons beyond the wafer thickness. Wade and Wood (2012) showed that this would be most significant for the heaviest elements of interest; in our case Ca, Ti and Fe. First, it is observed that TiO_2 contents are actually increased relative to the starting materials (Table S-1), suggesting no significant ‘unmeasured’ TiO_2 . Although CaO contents are decreased relative to the starting composition, this is due to the crystallisation of Ca-perovskite close to the melt - solid interface, forming a characteristic CaO-, SiO_2 -enriched and FeO-, Al_2O_3 -depleted rim (Fig. S-1 to S-3; see also Tagawa *et al.*, 2021). We therefore concluded that none of the EPMA measurements were affected by wafer thickness issues. The low total of ESS-DAC-7 is therefore also not related to wafer thickness issues, but perhaps by some Na_2O loss under the beam. It should be noted that the majority of literature SCSS experiments have low totals – the compiled dataset of Steenstra *et al.* (2018) yields an average of 98.70 ± 1.61 (1SD) obtained for a wide variety of capsule types and set-ups – which is probably a result of the increased analytical challenges of measuring S-rich silicate melts (see Steenstra *et al.*, 2020a for a detailed discussion on this topic).

S.2 Evidence for Sulfide-saturation of Experimental Silicate Melts

For the application of our results, it is important to demonstrate that the silicate melts are indeed sulfide-saturated and that they do not simply represent a melt that fully consumed the available sulfide liquid at the heated spot. Several lines of evidence can be used to argue for sulfide saturation. The most important line of evidence that argues for sulfide saturation of the experimental silicate melts at high P - T is the sign and magnitude of the variation of the SCSS with the FeO content of the silicate melt (Fig. 2a). Although there are slight P - T differences between the experiments, the SCSS versus wt. % FeO slope is very similar to/within error of systematic low pressure experimental observations by Wykes *et al.* (2015). The slope is also consistent with theoretical thermodynamic considerations of the increased dominance of the sulfide capacity term over other terms at higher FeO contents (>4 wt. % FeO; Wykes *et al.*, 2015). Given the fact that post-run FeS generally migrated to the edges of the heated spot, suggests the silicate melt either equilibrated with sulfide through liquid channels or that when it segregates it leaves a sulfide-saturated melt. The latter would be consistent with the expected, extremely fast diffusion of S in silicate melts at the very high temperatures of the experiments (Zhang *et al.*, 2010). In the unlikely case that the experimental silicate melts were not sulfide-saturated at high P - T conditions, our results provide important lower limits which are already are dramatically higher than modeled values using previous SCSS models. Finally, sulfide liquids generally migrated from the heated spot to colder areas, so that it cannot be excluded that FeS liquids initially present at peak conditions have slightly lower S contents relative to stoichiometric FeS ($x_{\text{FeS}} < 1$). As SCSS increases with x_{FeS} (*e.g.* Smythe *et al.*, 2017), any deviation from $x_{\text{FeS}} = 1$ would only further increase the relative differences between low- and high pressure results.

S.3 Correcting SCSS Values for Variable Silicate Melt FeO Contents

To unravel the effects of P - T on the SCSS, the data from this study and previous literature data from otherwise highly similar compositions should be normalised to a common FeO content, as FeO is by far the most important silicate melt compositional variable affecting the SCSS (*e.g.* O’Neil and Mavrogenes, 2002). We therefore used the FeO term from Table 5 of Steenstra *et al.* (2018) ($CX_{\text{Fe}} = 2.15(40)$), which was



derived from consideration of an extensive SCSS dataset ($N = 337$) and also incorporated sulfide compositional effects. Both the literature data and our newly derived high P - T data was normalised to $x_{\text{FeO}}^{\text{sil melt}} = 0.05$, corresponding to 8.1 wt. % FeO i.e. the FeO content of the present-day terrestrial primitive mantle (Palme and O'Neill, 2014). To incorporate any uncertainties arising from this correction, we propagated the uncertainties on both the FeO parameter from Steenstra *et al.* (2018) and on the actual measured SCSS values. This increased the uncertainties of the new high P - T SCSS values by 150 to 300 ppm, depending on the experiment. It should be noted that the SCSS does not vary significantly (200–300 ppm) between approximately 2 to 8 wt. % FeO, virtually the full range of potential FeO contents during terrestrial magma ocean crystallisation, as this is the minimum of the parabolic behavior describing SCSS as a function of FeO content (Wykes *et al.*, 2015; Fig. 2a in the main text).

S.4 Non FeO-compositional Effects on Derived SCSS Values

A MORB composition was chosen for the experiments because of its relatively low melting temperature and propensity for quenching to a glass (*e.g.* Suer *et al.*, 2017; Mahan *et al.*, 2018). The MORB composition (Gale *et al.*, 2013) used in our study is, however, significantly different than the expected composition of a primitive terrestrial magma ocean liquid or the primitive mantle (*e.g.* Palme and O'Neill, 2014). It should be noted that differences in FeO contents between our experiments and previous studies were taken into account by applying the FeO correction term from Steenstra *et al.* (2018), which is $CX_{\text{Fe}} = 2.15(40)$ (see section S.3). Note that the magnitude of the FeO effect is very similar for all previous SCSS models (*e.g.* Smythe *et al.*, 2017; Ding *et al.*, 2018; Steenstra *et al.*, 2018). Using the Smythe *et al.* (2017) model, we calculate the potential difference for an 8.1 wt. % FeO bearing primitive mantle melt (assuming the primitive mantle or PM composition from Palme and O'Neill, 2014) and compare the calculated SCSS value with SCSS values calculated for our experimental liquid compositions, normalised to 8.1 wt. % FeO. These calculations at 1 GPa and 1873 K suggests that the PM SCSS value is 850–1220 ppm higher than for the experimental liquid compositions. The SCSS for a peridotite-type liquid would thus only be slightly higher at the experimental P - T conditions, and confirms FeO is the main silicate melt compositional parameter affecting the SCSS, consistent with previous observations (*e.g.* Wykes *et al.*, 2015; Steenstra *et al.*, 2020a).

S.5 Dataset used for Parameterisations

To remove any potential effects arising from different silicate melt compositions, we use the following criteria and exclude the following literature data from our statistical database (1) H_2O -rich SCSS experiments, as each wt. % H_2O will result in an approximate increase of the SCSS by 100 ppm (Fortin *et al.*, 2015); (2) all SCSS data for silicate melts with <2.5 wt. % FeO due to the anomalous slope of SCSS versus FeO at low FeO contents (*e.g.* Wykes *et al.*, 2015; Steenstra *et al.*, 2020b); (3) all SCSS data for silicate melts with >2.5 wt. % TiO_2 due to the effects of high-Ti contents on the slope of SCSS with FeO (O'Neill and Mavrogenes, 2002); (4) all SCSS data for silicate melts with >55 wt. % SiO_2 due to the effects of SiO_2 on the SCSS (*e.g.* O'Neill and Mavrogenes, 2002; Smythe *et al.*, 2017; Steenstra *et al.*, 2018); (5) all SCSS data with >2.6 wt. % of alkalis due to their negative effects on the SCSS (D'Souza and Canil, 2018); (6) all SCSS data for silicate melts that have more than ± 5 wt. % CaO, Al_2O_3 and ± 2.5 wt. % MgO difference between the average compositions of our experiments; (7) all SCSS data for Fe-S liquid with <30 wt. % S due to the negative effects of lower sulfide x_{FeS} on the SCSS (Smythe *et al.*, 2017) and (8) all SCSS data for Fe-S liquid with > ± 6 wt. % of trace elements due to the negative effects of lower x_{FeS} on the SCSS, which may vary with the type of element considered. In the end, 42 SCSS values were included in the regression, with an overall P - T range of 1 atm to 40 GPa and $T = 1573$ – 4605 K, which are listed in Supplementary Table S-1.



S.6 Modelling Approach

To model the SCSS in a deep terrestrial magma ocean, we used main-text Eq. 2 in conjunction with the multi-stage core formation model (#S1) reported by Tagawa *et al.* (2021), which was directly based on the Rubie *et al.* (2015) model. Equation 2 is based on a primitive mantle content of 8.1 wt. % FeO and does not include an FeO term, as the SCSS does not deviate significantly within the FeO range relevant for the terrestrial magma ocean (*e.g.* Rubie *et al.*, 2015). It should be noted that in the latter models the FeO content is slightly lower in the first few % of magma ocean crystallisation if highly reduced accretion is assumed to have occurred early. This could hypothetically yield somewhat different SCSS values within the first few % of terrestrial accretion, but at this stage S contents are low and the SCSS would only be increased relative to higher FeO contents, making sulfide saturation also highly unlikely at this stage. The assumed geotherms, taken from Rubie *et al.* (2015) and required for calculating the SCSS values in Fig. 3a-b are based on liquidus/solidus data and were specifically calibrated for modeling the geotherms for magma ocean pressures below and above 24 GPa, respectively:

$$P < 24 \text{ GPa: } T_e = 1874 + 55.43P - 1.74P^2 + 0.0193P^3 \quad \text{Eq. (S-2)}$$

$$P \geq 24 \text{ GPa: } T_e = 1249 + 58.28P - 0.395P^2 + 0.0011P^3 \quad \text{Eq. (S-3)}$$

The modelled limit of 80 GPa corresponds with the proposed maximal pressure for a basal magma ocean (De Vries *et al.*, 2016). We incorporated the S mantle evolution model depicted in Fig. 1 from Rubie *et al.* (2015), as well as the models from Suer *et al.* (2017), which are based on either homogeneous or heterogeneous accretion. We compare these estimates with the modeled SCSS values (Eq. 2) while assuming different effective pressures of sulfide saturation, as a function of accreted mass %. The pressure versus accreted mass relationship was taken from Tagawa *et al.* (2021).

Rubie *et al.* (2015) defined the following equation for the average effective pressure of sulfide saturation, as sulfide segregation may occur at different depths in the magma ocean at a given stage of accretion:

$$P_{\text{eq-S}} = k_S \times \text{PCMB} \quad \text{Eq. (S-4)}$$

where PCMB is the core-mantle boundary pressure at the time of each FeS exsolution event, and k_S is a constant (Rubie *et al.*, 2015).



Supplementary Tables

Table S-1 Composition of the silicate starting glass and experimentally produced melts as measured by electron microprobe. *N* represents the number of analyses.

	SiO₂ (wt. %)	MgO	Al₂O₃	CaO	FeO	TiO₂	Na₂O	K₂O	CuO	CdO	ReO₂	S	Sum	<i>N</i>
Silicate melts														
Starting composition	48.48(14)	7.88(4)	15.17(3)	11.43(4)	9.79(5)	1.70(1)	2.54(2)	0.156(4)	–	–	–	–	97.36(15)	15
ESS-DAC-4	43.43(72)	8.63(18)	18.42(33)	7.94(6)	12.59(26)	1.89(2)	1.52(47)	0.135(5)	0.95(3)	–	0.05(3)	0.70(4)	96.25(96)	5
ESS-DAC-5	36.02(50)	8.48(11)	22.63(31)	6.51(8)	18.05(59)	1.44(2)	1.58(3)	0.066(4)	1.18(3)	–	0.10(6)	1.08(21)	97.14(63)	19
ESS-DAC-7	34.00(28)	7.69(7)	13.15(17)	6.85(6)	26.54(43)	2.32(1)	1.92(2)	0.144(3)	0.02(1)	0.286(4)	0.03(1)	1.18(8)	94.12(16)	32
	Fe (wt. %)	S	Na	Mg	Si	Al	Ca	Ti	Cu	Re	Se	O	Sum	<i>N</i>
Sulfide liquid														
ESS-DAC-4	55.89(381)	26.32(176)	0.26(18)	0.31(13)	1.09(146)	1.20(55)	0.52(72)	0.09(4)	1.35(158)	0.21(22)	n.d.	6.23(188)	93.68(214)	3

Table S-2 Compilation of used literature data.

Table S-2 is available for download (Excel) at <https://doi.org/10.7185/geochemlet.2219>



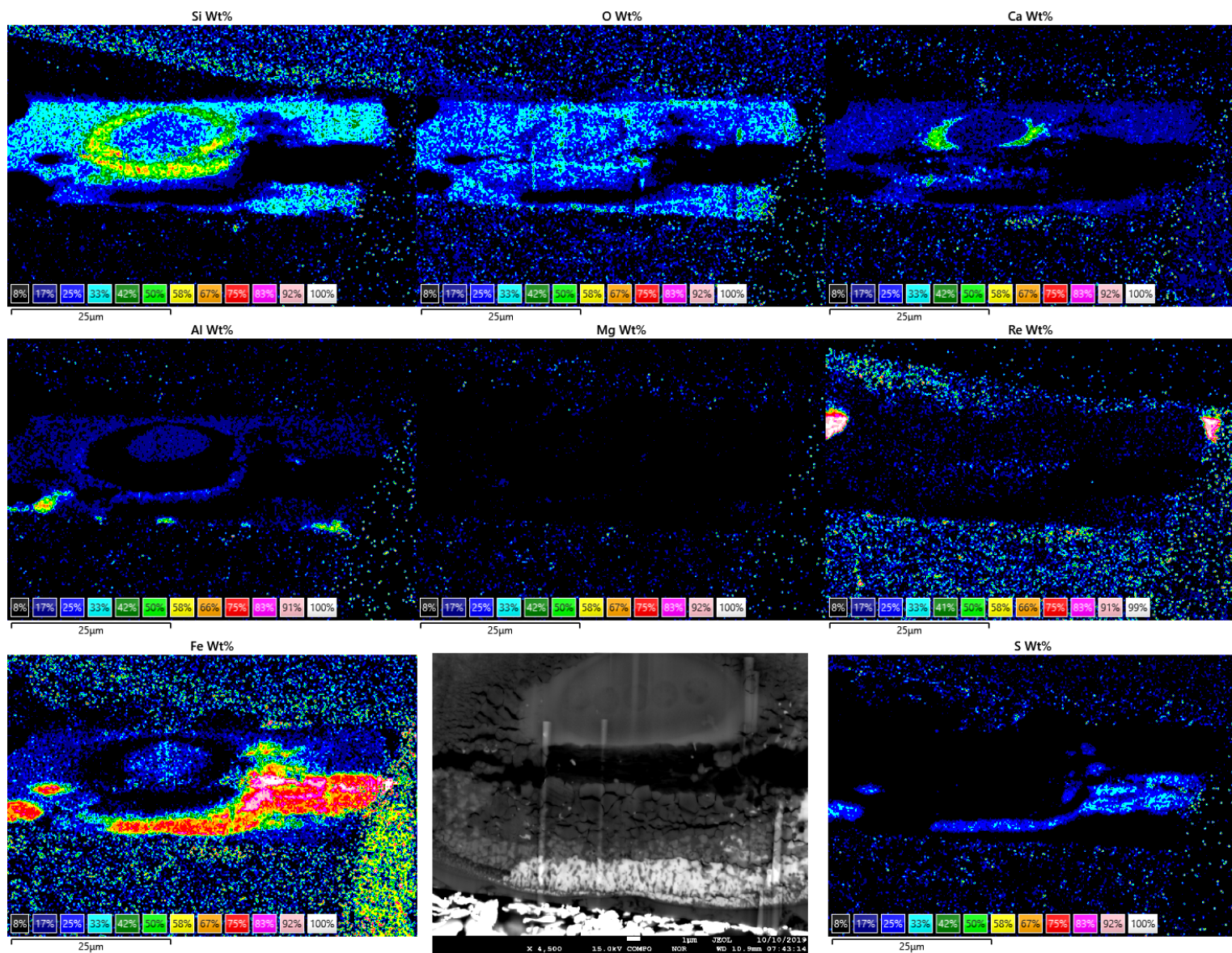


Figure S-1 Elemental EDS maps of experiment ESS-4-DAC.

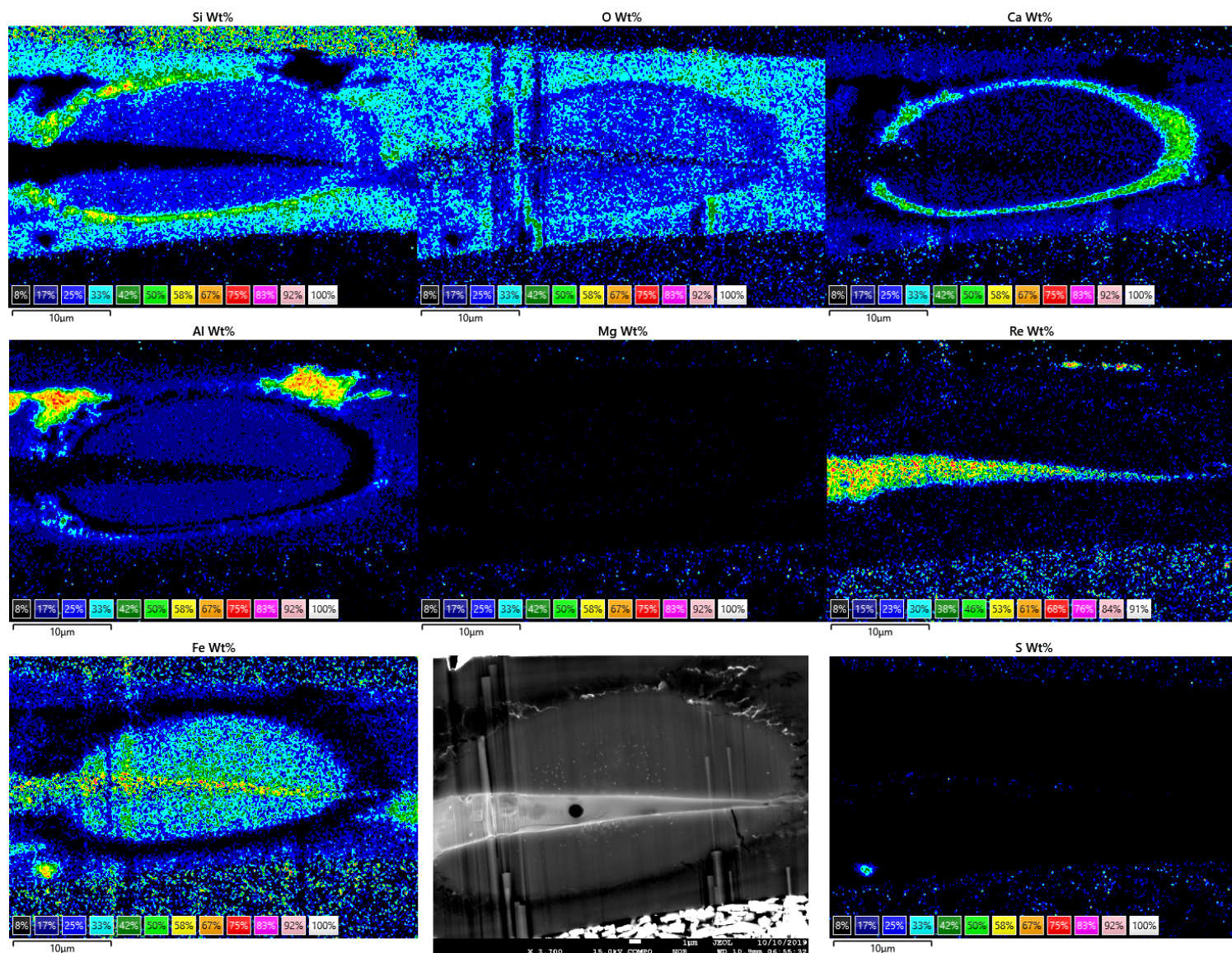


Figure S-2 Elemental EDS maps of experiment ESS-5-DAC.

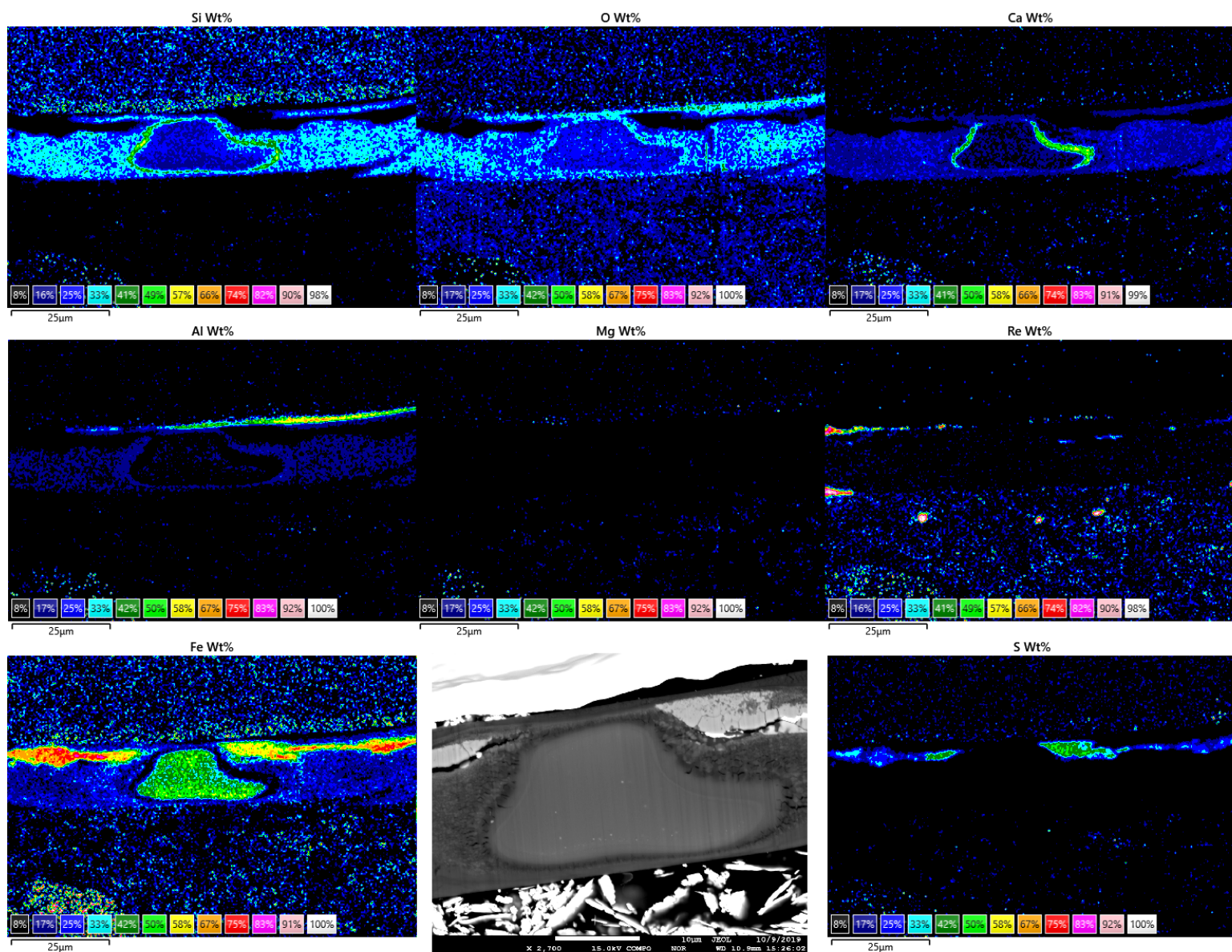


Figure S-3 Elemental EDS maps of experiment ESS-7-DAC.

Supplementary Information References

- De Vries, J., Nimmo, F., Melosh, H.J., Jacobson, S.A., Morbidelli, A., Rubie, D.C. (2016) Impact-induced melting during accretion of the Earth. *Progress in Earth and Planetary Science* 3, 7. <https://doi.org/10.1186/s40645-016-0083-8>
- Ding, S., Hough, T., Dasgupta, R. (2018) New high-pressure experiments on sulfide saturation of high-FeO* basalts with variable TiO₂ contents - Implications for the sulfur inventory of the lunar interior. *Geochimica et Cosmochimica Acta* 222, 319–339. <https://doi.org/10.1016/j.gca.2017.10.025>
- D'Souza, R.J., Canil, D. (2018) Effect of alkalinity on sulfur concentration at sulfide saturation in hydrous basaltic andesite to shoshonite melts at 1270°C and 1 GPa. *American Mineralogist* 103, 1030–1043. <https://doi.org/10.2138/am-2018-6404>
- Fortin, M.-A., Riddle, J., Desjardins-Langlais, Y., Baker, D.R. (2015) The effect of water on the sulfur concentration at sulfide saturation (SCSS) in natural melts. *Geochimica et Cosmochimica Acta* 160, 100–116. <https://doi.org/10.1016/j.gca.2015.03.022>
- Gale, A., Dalton, C.A., Langmuir, C.H., Su, Y., Schilling, J.-G. (2013) The mean composition of ocean ridge basalts. *Geochemistry Geophysics Geosystems* 14, 489–518. <https://doi.org/10.1029/2012GC004334>
- Jugo, P.J., Luth, R.W., Richards, J.P. (2005) An experimental study of the sulfur content in basaltic melts saturated with immiscible sulfide or sulfate liquids at 1300°C and 1 GPa. *Journal of Petrology* 46, 783–798. <https://doi.org/10.1093/petrology/egh097>
- Kiseeva, E.S., Wood, B.J. (2013) A simple model for chalcophile element partitioning between sulphide and silicate liquids with geochemical applications. *Earth and Planetary Science Letters* 383, 68–81. <https://doi.org/10.1016/j.epsl.2013.09.034>
- Kiseeva, E.S., Wood, B.J. (2015) The effects of composition and temperature on chalcophile and lithophile element partitioning into magmatic sulphides. *Earth and Planetary Science Letters* 424, 280–294. <https://doi.org/10.1016/j.epsl.2015.05.012>
- Lord, O.T., Wann, E.T.H., Hunt, S.A., Walker, A.M., Santangeli, J., Walter, M.J., Dobson, D.P., Wood, I.G., Vocadlo, L., Morard, G., Mezouar, M. (2014) The NiSi melting curve to 70 GPa. *Physics of the Earth and Planetary Interiors* 233, 13–23. <https://doi.org/10.1016/j.pepi.2014.05.005>
- Mahan, B., Siebert, J., Blanchard, I., Badro, J., Kubik, E., Sossi, P., Moynier, F. (2018) Investigating Earth's formation history through copper and sulfur metal-silicate partitioning during core-mantle differentiation. *Journal of Geophysical Research: Solid Earth* 123, 8349–8363. <https://doi.org/10.1029/2018JB015991>
- O'Neil, H.St.C., Mavrogenes J.A. (2002) The sulfide capacity and the sulfur content at sulfide saturation of silicate melts at 1400°C and 1 bar. *Journal of Petrology* 43, 1049–1087. <https://doi.org/10.1093/petrology/43.6.1049>
- Palme, H., O'Neill, H.St.C (2014) 3.1 - Cosmochemical estimates of mantle composition. In: Holland, H.D., Turekian, K.K. (Eds.) *Planets, Asteroids, Comets and The Solar System, Treatise of Geochemistry (Second Edition)*. Elsevier, Oxford, 1–39. <https://doi.org/10.1016/B978-0-08-095975-7.00201-1>
- Peach, C.L., Mathez, E.A. (1993) Sulfide melt-silicate melt distribution coefficients for nickel and iron and implications for the distribution of other chalcophile elements. *Geochimica et Cosmochimica Acta* 57, 3013–3021.
- Rubie, D.C., Jacobson, S.A., Morbidelli, A., O'Brien, D.P., Young, E.D., de Vries, J., Nimmo, F., Palme, H., Frost, D.J. (2015) Accretion and differentiation of the terrestrial planets with implications for the compositions of early-formed Solar System bodies and accretion of water. *Icarus* 248, 89–108. <https://doi.org/10.1016/j.icarus.2014.10.015>
- Siebert, J., Badro, J., Antonangeli, D., Ryerson, F.J. (2012) Metal-silicate partitioning of Ni and Co in a deep magma ocean. *Earth and Planetary Science Letters* 321, 189–197. <https://doi.org/10.1016/j.epsl.2012.01.013>
- Smythe, D.J., Wood, B.J., Kiseeva, E.S. (2017) The S content of silicate melts at sulfide saturation: New experiments and a model incorporating the effects of sulfide composition. *American Mineralogist* 102, 795–803. <https://doi.org/10.2138/am-2017-5800CCBY>
- Steenstra, E.S., Seegers, A.X., Eising, J., Tomassen, B.G.J., Webers, F.P.F., Berndt, J., Klemme, S., Matveev, S., van Westrenen, W. (2018) Evidence for a sulfur undersaturated lunar interior from the solubility of sulfur in lunar melts and sulfide-silicate partitioning of siderophile elements. *Geochimica et Cosmochimica Acta* 231, 130–156. <https://doi.org/10.1016/j.gca.2018.04.008>
- Steenstra, E.S., Berndt, J., Klemme, S., Snape, J.F., Bullock, E.S., van Westrenen, W. (2020a) The fate of sulfur and chalcophile elements during crystallization of the lunar magma ocean. *Journal of Geophysical Research: Planets* 125, e2019JE006328. <https://doi.org/10.1029/2019JE006328>
- Steenstra, E. S., Trautner, V. T., Berndt, J., Klemme, S., van Westrenen, W. (2020b) Trace element partitioning between sulfides, metals and silicate melts at highly reduced conditions: insights into the depletion of volatile elements during core formation in



- reduced bodies. *Icarus* 335, 113408. <https://doi.org/10.1016/j.icarus.2019.113408>
- Suer, T.-A., Siebert, J., Remusat, L., Menguy, N., Fiquet, G. (2017) A sulfur-poor terrestrial core inferred from metal-silicate partitioning experiments. *Earth and Planetary Science Letters* 469, 84–97. <https://doi.org/10.1016/j.epsl.2017.04.016>
- Tagawa, S., Sakamoto, N., Hirose, K., Yokoo, S., Hernlund, J., Ohishi, Y., Yurimoto, H. (2021) Experimental evidence for hydrogen incorporation into Earth's core. *Nature Communications* 12, 2588. <https://doi.org/10.1038/s41467-021-22035-0>
- Wade, J., Wood, B.J. (2012) Metal-silicate partitioning experiments in the diamond anvil cell: A comment on potential analytical errors. *Physics of the Earth and Planetary Interiors* 192–193, 54–58. <https://doi.org/10.1016/j.pepi.2011.12.002>
- Walter, M.J., Koga, K.T. (2004) The effect of chromatic dispersion on temperature measurement in the laser-heated diamond anvil cell. *Physics of the Earth and Planetary Interiors* 143–144, 541–558. <https://doi.org/10.1016/j.pepi.2003.09.019>
- Walter, M.J., Thomson, A.R., Wang, W., Lord, O.T., Ross, J., McMahon, S.C., Baron, M.A., Melekhova, E., Kleppe, A.K., Kohn, S.C. (2015) The stability of hydrous silicates in Earth's lower mantle: Experimental constraints from the systems MgO-SiO₂-H₂O and MgO-Al₂O₃-SiO₂-H₂O. *Chemical Geology* 418, 16-29. <https://doi.org/10.1016/j.chemgeo.2015.05.001>
- Wykes, J.L., O'Neill, H.St.C., Mavrogenes, J.A. (2015) The effect of FeO on the sulfur content at sulfide saturation (SCSS) and the selenium content at selenide saturation of silicate melts. *Journal of Petrology* 56, 1407–1424. <https://doi.org/10.1093/petrology/egv041>
- Zhang, Y., Ni, H., Chen, Y. (2010) Diffusion data in silicate melts. *Reviews in Mineralogy and Geochemistry* 72, 311–408. <https://doi.org/10.2138/rmg.2010.72.8>

